

A Determination of H_0 with the CLASS Gravitational Lens B1608+656: III. A Significant Improvement in the Precision of the Time Delay Measurements

C. D. Fassnacht

*Space Telescope Science Institute, 3700 San Martin Drive, Baltimore, MD 21218;
and National Radio Astronomy Observatory, P.O. Box O, Socorro, NM 87801*

`cdf@stsci.edu`

E. Xanthopoulos

University of Manchester, Jodrell Bank Observatory, Macclesfield, Cheshire SK11 9DL, UK.

`emily@jb.man.ac.uk`

L. V. E. Koopmans

Theoretical Astrophysics, California Institute of Technology, 130-33, Pasadena, CA 91125.

`leon@tapir.caltech.edu`

and

D. Rusin

Harvard-Smithsonian Center for Astrophysics, 60 Garden Street, Cambridge, MA 02138.

`drusin@cfa.harvard.edu`

ABSTRACT

The gravitational lens CLASS B1608+656 is the only four-image lens system for which all three independent time delays have been measured. This makes the system an excellent candidate for a high-quality determination of H_0 at cosmological distances. However, the original measurements of the time delays had large (12–20%) uncertainties, due to the low level of variability of the background source during the monitoring campaign. In this paper, we present results from two additional VLA monitoring campaigns. In contrast to the $\sim 5\%$ variations seen during the first season of monitoring, the source flux density changed by 25–30% in each of the subsequent two seasons. We analyzed the combined data set from all three seasons of monitoring to improve significantly the precision of the time delay measurements; the delays are consistent with those found in the original measurements, but the uncertainties have decreased by factors of two to three. We combined the delays with revised isothermal mass models to derive a measurement of H_0 . Depending on the positions of the galaxy centroids, which vary by up to $0''.1$

in HST images obtained with different filters, we obtain $H_0 = 61\text{--}65 \text{ km s}^{-1} \text{ Mpc}^{-1}$, for $(\Omega_M, \Omega_\Lambda) = (0.3, 0.7)$. The value of H_0 decreases by 6% if $(\Omega_M, \Omega_\Lambda) = (1.0, 0.0)$. The formal uncertainties on H_0 due to the time delay measurements are ± 1 (± 2) $\text{km s}^{-1} \text{ Mpc}^{-1}$ for the 1σ (2σ) confidence limits. Thus, the systematic uncertainties due to the lens model, which are on the order of $\pm 15 \text{ km s}^{-1} \text{ Mpc}^{-1}$, now dominate the error budget for this system. In order to improve the measurement of H_0 with this lens, new models that incorporate the constraints provided by stellar dynamics and the optical/infrared Einstein ring seen in HST images must be developed.

Subject headings: distance scale — galaxies: individual (B1608+656) — gravitational lensing

1. Introduction

Gravitational lenses provide excellent tools for the study of cosmology. In particular, the method developed by Refsdal (1964) can be used to determine the Hubble Constant at cosmological distances. This method requires a lens system for which both lens and source redshifts have been measured, for which a well-constrained model of the gravitational potential of the lensing mass distribution has been determined, and for which the time delays between the lensed images have been measured. To date, measurements of time delays have been reported in the literature for 11 lens systems: 0957+561 (Kundić et al. 1995, 1997c), PG 1115+080 (Schechter et al. 1997; Barkana 1997), JVAS B0218+357 (Biggs et al. 1999; Cohen et al. 2000), PKS 1830-211 (Lovell et al. 1998; Wiklind & Combes 2001), CLASS B1608+656 (Fassnacht et al. 1999, hereafter Paper I), CLASS B1600+434 (Koopmans et al. 2000; Burud et al. 2000), JVAS B1422+231 (Patnaik & Narasimha 2001), HE 1104-1805 (Gil-Merino, Wisotzki, & Wambsganss 2002, see, however, Pelt, Refsdal, & Stabell 2002), HE 2149-2745 (Burud et al. 2002a), RX J0911.4+0551 (Hjorth et al. 2002), and SBS 1520+530 (Burud et al. 2002b). Of these lens systems, CLASS B1608+656 is the only four-image system for which all three independent time delays have been unambiguously measured.

The CLASS B1608+656 lens system consists of the core of a radio-loud poststarburst galaxy at a redshift of $z = 1.394$ (Fassnacht et al. 1996) being lensed by a $z = 0.630$ pair of galaxies (Myers et al. 1995). Radio maps of the system show four images of the background source arranged in a typical lens geometry (Figure 1). Models of the lens system predict that, if the background source is variable, image B should show the variation first, followed by components A, C, and D in turn (Myers et al. 1995; Koopmans & Fassnacht 1999, hereafter Paper II). The time delays determined in Paper I were based on radio-wavelength light curves obtained with the Very Large Array (VLA)¹

¹The National Radio Astronomy Observatory is a facility of the National Science Foundation operated under cooperative agreement by Associated Universities, Inc.

between 1996 October and 1997 May. During that time, the background source 8.5 GHz flux density varied by $\sim 5\%$. Although the measured time delays were robust, the small level of variability meant that the uncertainties on the delays were large. The estimated uncertainties from the Paper I data ranged from $\sim 12\%$ for the B \rightarrow D time delay (τ_{BD}) to $\sim 20\%$ for the other two measured delays (95% CL). These uncertainties translated to uncertainties on the derived value of the Hubble Constant of $\sim 15\%$ (Paper I). In addition, the lens modeling contributes an uncertainty of $\sim 30\%$ to the derived H_0 , with the largest contribution coming from the uncertainty in the radial profile of the mass distribution in the lensing galaxies (Paper II). In order to achieve a more precise determination of H_0 from this lens system, the uncertainties on both the time delays and the modeling need to be significantly reduced. This paper addresses the first of those issues.

2. Observations

In VLA test observations conducted before the start of the first monitoring program, the flux density of the B1608+656 components had varied by up to 20% on time scales of months. If detected during a monitoring program, variations on this scale would allow a significant reduction in the time delay uncertainties. Thus, we continued our monitoring program with the VLA. Our observations were conducted at 8.5 GHz. The angular resolution required to separate properly the individual images of the background source limited the observations to the times in which the VLA was in its most extended configurations, the A, BnA, and B arrays. Thus, we have light curves covering the approximately eight months out of every 16-month cycle, during which the VLA was in the proper configurations. We have denoted these eight-month blocks as observing “seasons,” with season 1 being 1996 November to 1997 May, which was discussed in Paper I.

In this paper, we present results from seasons 2 and 3. Table 1 summarizes the observations that were conducted. Each observing epoch contained observations of CLASS B1608+656; the phase calibrator, 1642+689; the primary flux calibrator, 3C 343 (1634+628); and secondary flux calibrators. The phase center for the observations of B1608+656 was chosen to be the approximate center of the system at RA: 16^h09^m13^s.953 and Dec: +65°32′28″.00 (J2000). Our primary flux calibrator is not a standard VLA flux calibrator. However, it is much closer in the sky to our lens system than the usual flux density calibrators, 3C 286 and 3C 48, and our season 1 observations showed that its flux density is stable (Paper I). Any errors in the absolute flux-density calibration due to either variability in this source or secondary instrumental effects could be corrected through the use of the secondary flux calibrators. These secondary calibrators are steep-spectrum radio sources and, as such, should not be highly variable. In particular, if the light curves of the secondary flux calibrators show variations that are correlated, it is almost certain that these variations are produced by flux calibration errors rather than being intrinsic. Thus, the information obtained from correlated variability of the secondary calibrators can be used to correct the light curves of the lensed images (see Paper I; also §3.4). Compact symmetric objects (CSOs) have been shown to be especially stable secondary calibrators at 8.5 GHz (Fassnacht & Taylor 2001, hereafter FT01). The

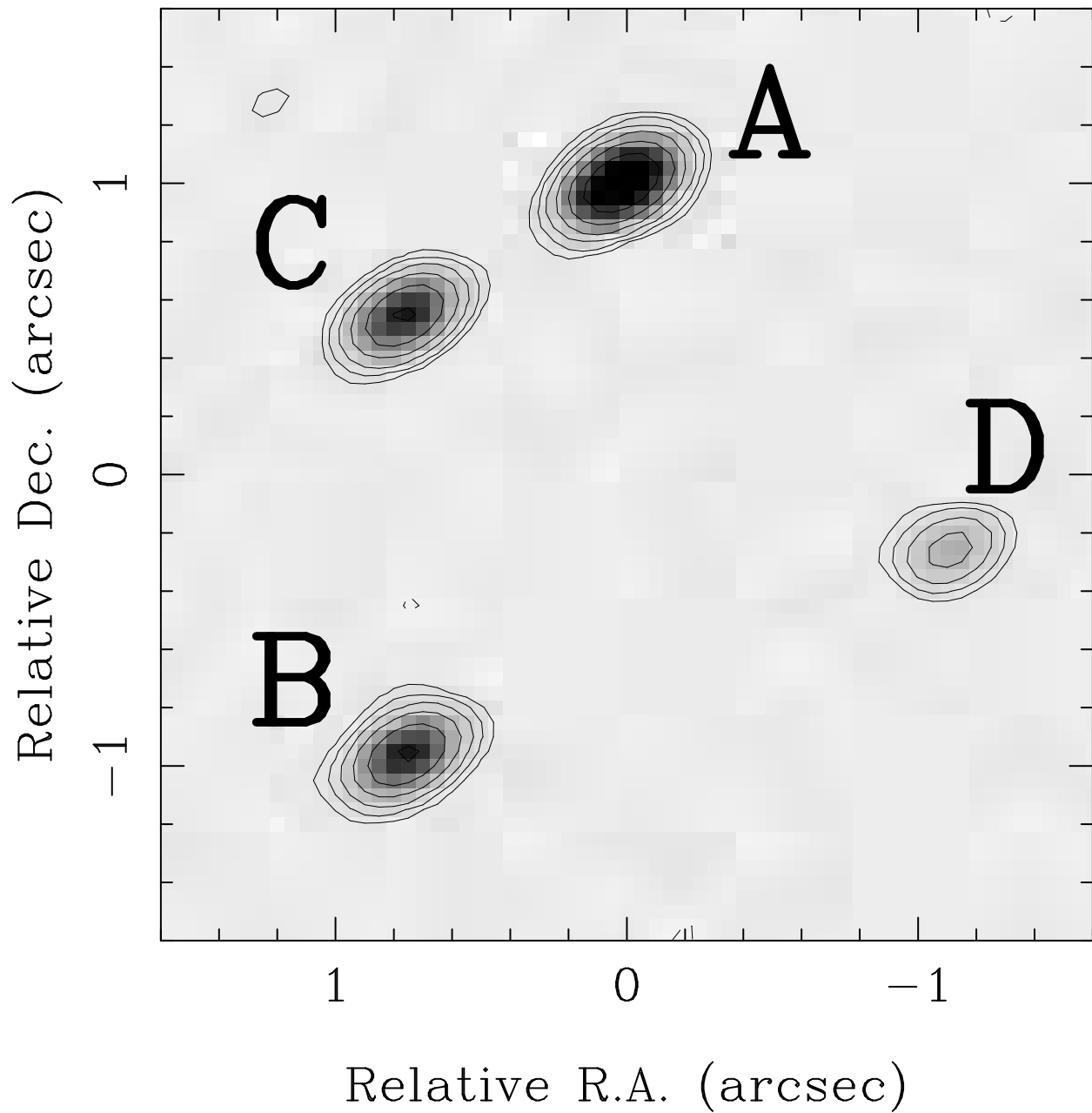


Fig. 1.— Typical radio map of B1608+656 from the season 3 monitoring campaign. These data were obtained on 1999 August 08. Both the grayscale and the contours represent radio brightness. The contours are set at -2.5 , 2.5 , 5 , 10 , 20 , 40 , 80 , and 160 times the RMS noise level of $0.13 \text{ mJy beam}^{-1}$.

season 2 secondary flux calibrators were 1633+741, which was used in the Paper I analysis, and two CSOs: J1400+6210 and J1944+5448. The integration times on the various sources were typically one minute on the phase calibrator and the CSOs, two minutes on 1633+741, and approximately five minutes on the lens system. Neither CSO was observed for the full length of season 2; J1944+5448 was observed from 1998 February 13 to 1998 June 01 while J1400+6210 was observed from 1998 May 12 to 1998 October 19. The observations for season 3 were similar to those of season 2, but with a different set of secondary flux calibrators. We dropped 1633+741 and J1944+5448 and added six CSOs to the two used in the season 2 observations. The increase in the number of good secondary flux calibrators provided a better estimate of the errors in the absolute flux density calibration. The additional CSOs used were: J1035+5628, J1148+5924, J1244+4048, J1545+4751, J1823+7938, and J1945+7055. Because there were more sources observed per epoch than in the first two seasons, the average integration time per source dropped slightly. The phase calibrator and CSOs typically were observed for 45-60 sec and B1608+656 was observed for a few minutes.

3. Data Reduction

3.1. Calibration

The data were calibrated using customized procedures that acted as an interface to tasks in the NRAO data reduction package, AIPS. For consistency, the data from all three observing seasons were calibrated in the same way. Therefore, the season 1 data were recalibrated. The overall flux density calibration was tied to 3C 343. As discussed in FT01, 3C 343 is not an ideal calibrator due to some low surface-brightness emission surrounding the central component. However, it was possible to correct for the changes in the total measured flux density of 3C 343 as the VLA configuration changed (see §3.4).

The calibration procedure for each epoch of observation began with careful data editing. Bad integrations on the calibrators, indicated by discrepant amplitudes or phases, were deleted. Any antenna which exhibited a large number of bad integrations during an epoch was flagged for the entire epoch. The antenna system temperatures were also used as a diagnostic to discover bad

Table 1. Monitoring Observations

Season	Start Date	End Date	N_{obs}	N_{good}	Average Spacing (d)
1	1996 Oct 10	1997 May 26	66	64	3.6
2	1998 Feb 13	1998 Oct 19	81	78	3.1
3	1999 Jun 15	2000 Feb 14	92	88	2.7

integrations, which were then flagged. One antenna in particular (antenna 3) had system temperatures that were, on average, a factor of three higher than those of the other antennas. Because this behavior was seen during all three seasons of observations, we flagged antenna 3 before doing any calibration. After the bad data had been flagged, the antenna gain phases and amplitudes were determined through self-calibration on the bright, compact calibrator sources. For all of the CSOs and the phase calibrator, we used a point source model to do the self calibration. The emission from two of the CSOs, J1035+5628 and J1400+6210, is slightly resolved so, for those sources, we imposed a maximum baseline length of $400 \text{ k}\lambda$ in the calculation of the gain solutions. The more complicated morphology of the flux calibrator required a simple model as the input to the self-calibration. Otherwise, the processing for the flux calibrator was the same as that used for the phase calibrator and CSOs. The self-calibration was conducted in two steps. In the first step, solutions were calculated for the gain phases only, with a solution interval of 10 sec. Those solutions were applied to the data and then the second calibration was performed. This time, both phase and amplitude solutions were calculated, with a solution interval of 30 sec. The flux-density scale was then transferred to the CSOs and phase calibrators through the GETJY task. Finally, the gain solutions from the phase calibrators were interpolated and applied to the data on B1608+656 and, for seasons 1 and 2, 1633+741.

3.2. Mapping and Initial Light Curves

The flux densities for the B1608+656 components, the CSOs, and 1633+741 were obtained through the use of the model-fitting procedures in the DIFMAP software package (Shepherd 1997). The process used to derive the flux densities for the CSOs was described in FT01. The flux densities for B1608+656 and 1633+741 were measured using methods similar to those described in Paper I, but with small variations. For 1633+741 the only change in the processing was to limit the (u, v) range used for the model-fitting procedure to include only baselines with lengths less than $400 \text{ k}\lambda$. This change de-emphasized the contribution of small-scale structure in the source, namely the emission associated with the probable core component. The data on the source suggested that the core of 1633+741 was variable during the observations. By minimizing the contribution of the core in the model-fitting, we obtained light curves which had less intrinsic scatter, especially in the A-configuration data, and which were much more consistent with the CSO light curves.

For B1608+656, we investigated the effect of letting the component positions vary during the model fitting. We ran the DIFMAP scripts twice, once with variable positions and once with the positions fixed at the values given in Table 2. For the case in which we let the positions vary, the best-fit positions returned by the model-fitting were very close to those in the fixed-position models. For all components the mean offsets from the fixed positions were 1 milliarcsecond (mas) or less. The RMS scatter about the mean ranged from 1 to 4 mas, with the largest RMS offsets being those associated with component D in seasons 2 and 3, when the component was faintest. The offsets are in all cases small compared to the VLA beam sizes of 250 to 700 mas. As expected for such small

positional differences, there were no significant differences in the flux densities obtained via the two fitting procedures. Thus, we chose to use only the results obtained by holding the positions fixed.

3.3. Light Curve Editing

During the course of the observations, there were some data sets obtained under less-than-ideal conditions. Although VLA observations at 8.5 GHz are relatively unaffected by poor weather, extreme weather conditions such as thunderstorms or very high winds can produce data which can not be properly calibrated given the observing strategy that we had used. Based on our evaluation of the success of the calibration procedure, we chose to delete a small number of epochs from the light curves. Paper I describes the reasons for flagging two bad epochs in season 1. In seasons 2 and 3 we flagged a total of 4 epochs due to bad weather conditions. We also flagged 3 points obtained at the very beginning of the seasons during which the VLA was in a mixed configuration while the antennas were being moved from their D-array positions to their A-array positions. For these epochs, the absolute flux density calibration was not correct. The number of epochs remaining after flagging the data from each season is listed in the N_{good} column of Table 1.

3.4. Correction of Systematic Errors and Final Light Curves

Paper I and FT01 describe a method that uses the light curves of steep-spectrum radio sources to correct for systematic errors in the absolute flux density calibration. We have followed the same method in this paper to correct the light curves of the lensed images. The results presented in FT01 showed that CSOs are excellent flux density calibrators at the frequencies used for our monitoring observations. As discussed in FT01, the light curves of J1823+7938 and J1945+7055 showed evidence of additional systematic effects not seen in the light curves of the other CSOs. Thus, those two sources were not included in the construction of the season 3 correction curve. Additionally, the season 2 data show that 1633+741, although relatively stable, has noisier light curves than those of the CSOs. This is probably due to the significant extended emission and complicated morphology of 1633+741. Our snapshot observations did not cover the (u, v) plane well enough to accurately model the complex emission of the source. Thus, we dropped 1633+741 as a secondary flux density calibrator.

There were two details to consider in constructing the correction curves. The first was that the primary flux calibrator, 3C 343 has some extended emission. The B-configuration observations are more sensitive to lower surface brightness emission than are the A-configuration observations. Thus, the total flux density observed for 3C 343 will increase whenever the VLA enters the B configuration. The observations of the secondary flux calibrators were used to examine the size of this effect. The effect only appeared to be significant during season 3, perhaps because the brightness of the central component had decreased slightly and the extended emission thus contributed a larger percentage

to the total B-configuration flux density. To ensure that the correction curves did not include any step function introduced by the changing flux density of 3C 343, we computed for each season the mean flux densities of the CSOs in the A, BnA, and B configurations separately and used those values to normalize the light curves. This procedure also corrected for any step functions caused by the presence of low-level extended emission in the secondary flux calibrators themselves. The second detail to consider was that, by dropping 1633+741, we had no secondary flux density calibrators for the recalibrated season 1 data. However, our analysis of the light curves and the time delay results showed that the inclusion of the 1633+741 data introduced more scatter than it took out. Thus, we believe that our decision to drop the 1633+741 data was the proper one.

The final corrected light curves for the four components in B1608+656 are shown in Figure 2. The errors on the points are a combination in quadrature of (1) the RMS noise in the residual map from the DIFMAP processing, typically ~ 0.1 mJy beam $^{-1}$, and (2) a 0.6% fractional uncertainty arising from errors in the absolute flux density calibration. We have estimated the fractional uncertainty from the season 3 CSO light curves. All of the light curves have been normalized by their mean flux densities over the entire three seasons of observations. Thus, the plot in Figure 2 represents the fractional variations in flux density, which allows for direct comparison of the component light curves. The figures show that the background source varied significantly in both season 2 and season 3. The variations in each of these seasons are on the order of 25–30%, in contrast to the $\sim 5\%$ variations seen in season 1. Unfortunately, the season 2 light curves have nearly a constant slope, which made it difficult to determine unambiguously the time delays and magnifications needed to align the component light curves. However, the season 3 light curves have both a large amount of variation and clear changes in slope, making them excellent inputs for determining time delays.

4. Determination of Time Delays

4.1. Dispersion Method

In Paper I we used several statistical methods to determine the delays between the light curves. In this paper, with obvious source variability and ~ 250 points in the light curves of each component, we have used only the dispersion method described by Pelt et al. (1994, 1996). This method has the clear advantage of not requiring any interpolation of the input light curves. As we did in Paper I, we used the D_2^2 and $D_{4,2}^2$ methods (as defined in Pelt et al. 1996) to compare the three independent pairs of light curves. In these methods, one of the input light curves is shifted in time by a delay (τ), scaled in flux by a relative magnification (μ), and combined with the second curve to create a composite light curve. The internal dispersion in the composite curve is then calculated by computing the weighted sum of the squared flux difference between pairs of points in the curve. For the D_2^2 method, only adjacent pairs of points are considered, while, for the $D_{4,2}^2$ method, additional pairs of points are considered. In the $D_{4,2}^2$ calculations, all pairs separated by fewer than δ days contribute to the final dispersion, but with an additional weighting such that the

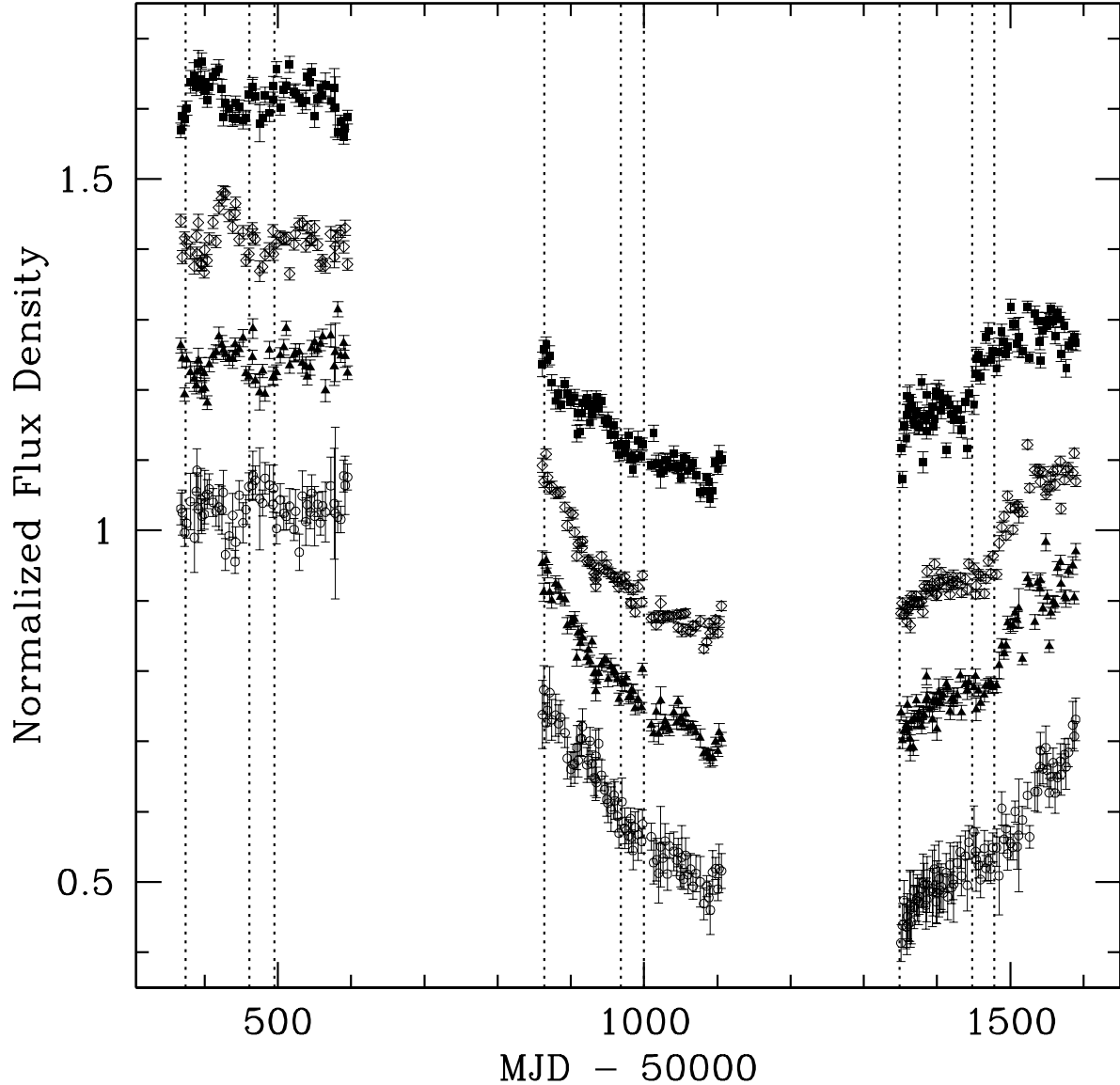


Fig. 2.— Normalized light curves of the four lensed images of the background radio source in the CLASS B1608+656 lens system obtained over the three observing seasons. From top to bottom, the curves correspond to components B (filled squares), A (open diamonds), C (filled triangles), and D (open circles). The abscissa is time, with units of MJD – 50000. Each curve has been normalized by its mean flux density over the course of the observations, so the plotted points represent fractional changes in the component flux densities. For clarity, each light curve has been shifted vertically by an arbitrary amount. The component B light curve has been shifted by +0.3, the component A curve by +0.08, the component C curve by –0.08, and the component D curve by –0.30. For each season, the vertical dotted lines delineate the times at which the VLA configuration changed: D→A, A→BnA, and BnA→B, from left to right. The gaps in the curves correspond to times in which the VLA was in the BnC, C, CnD, and D-arrays, during which the angular resolution provided by the array was not high enough to cleanly resolve the four components in the system.

pairs with the smallest separation in time have the highest weights. By including more pairs, the $D_{4,2}^2$ statistic is less likely to be affected by individual discrepant points.

We searched a range of delays and relative magnifications to determine the values that, when applied to one of the input curves, produced the best alignment between the two curves (i.e., the lowest internal dispersion in the composite curve). The (μ, τ) pairs used for the search formed regular grids. The τ values were separated by 0.5 d in the range $\tau_0 \pm 30$ d. The values of τ_0 were those derived in Paper I, namely 31, 36, and 76 d. The range of relative magnifications searched was $0.95\mu_0$ to $1.05\mu_0$, with steps of size $\Delta\mu = 0.001\mu_0$. The values of μ_0 were also chosen to match the best-fit values obtained from the season 1 data: 2.042, 1.038, and 0.351 for μ_{AB} , μ_{CB} , and μ_{DB} , respectively. Here, we have defined μ_{AB} as the relative magnification of component A with respect to component B, and so forth. These relative magnifications express the ratios of the component flux densities, once the light curves have been properly corrected for the time delays.

4.2. Delays from Combined Analysis

As a first step in the determination of the delays, we analyzed the results from each season individually. The results from season 2 were not conclusive due to the degeneracy between the relative magnification and the time delay. However, the season 1 and season 3 light curves gave robust determinations of the time delays and relative magnifications between the curves. The delays determined from the two seasons were consistent, but the magnifications were discrepant. It is possible that the absolute flux density scale might change from season to season. However, such a change would manifest itself as a constant scaling applied to each of the component flux densities equally, leaving the relative magnifications unaffected. We thus concluded that some slow process had affected the measured flux density of at least one of the images (see §6.1). As a result, our approach to the combined analysis of the data from all three seasons changed. Instead of finding a set of best-fit global magnifications, we let the relative magnifications vary from season to season. Because the determination of the dispersion is an additive process, the implementation of this change was straightforward. Consider the comparison of two light curves, Q_i and R_j , which are sampled only during the three seasons defined by the ranges $[t_{1,0}, t_{1,f}]$, $[t_{2,0}, t_{2,f}]$, and $[t_{3,0}, t_{3,f}]$. The composite curve $T_k(t_k)$ was constructed from the input curves, with the second curve shifted in time by a delay τ and scaled by season-dependent relative magnifications μ_n , such that

$$T_k = \begin{cases} Q_i, & \text{if } t_k = t_i \\ R_j/\mu_1, & \text{if } t_k = (t_j - \tau) \text{ and } t_{1,0} \leq t_j \leq t_{1,f} \\ R_j/\mu_2, & \text{if } t_k = (t_j - \tau) \text{ and } t_{2,0} \leq t_j \leq t_{2,f} \\ R_j/\mu_3, & \text{if } t_k = (t_j - \tau) \text{ and } t_{3,0} \leq t_j \leq t_{3,f}. \end{cases} \quad (1)$$

The internal dispersion in the composite curve was then calculated in the standard fashion described above.

For each pair of curves, we searched a grid of $(\mu_1, \mu_2, \mu_3, \tau)$ values to find the combination

which gave the lowest dispersion. In order to ascertain the robustness of the derived time delays, we repeated the $D_{4,2}^2$ method with a range of values for δ and compared the results (Table 3). Figure 3 shows typical output curves from the dispersion analysis. We show for comparison the equivalent curves from the Paper I analysis as dashed lines on the plots. Although both sets of curves give nearly the same time delays, the curves associated with the combined data sets show much clearer minima.

We have taken the median values of the columns in Table 3 to be the best-fit time delays and relative magnifications as determined from the data. These values are given in Table 4. The median time delays are $\tau_{BA} = 31.5$ d, $\tau_{BC} = 36.0$ d, and $\tau_{BD} = 77.0$ d. The time delay ratios are $(\tau_{BD}/\tau_{BA}) = 2.44$ and $(\tau_{BD}/\tau_{BC}) = 2.14$. These agree well with the values obtained in Paper I.

We performed several consistency checks on the derived delays. First, we computed all possible delays between a leading component and a trailing component, using the dispersion methods listed in Table 3. The median values obtained for these delays were $\tau_{AC} = 2.5$ d, $\tau_{AD} = 45.5$ d, and $\tau_{CD} = 44.0$ d. These delays are consistent within the uncertainties (§5) with the three delays calculated above. Secondly, we computed the delays between component B and the other three components using the χ^2 -minimization technique described in Paper I, which requires that the input light curves be interpolated onto a regularly-spaced grid. The χ^2 -minimization results were consistent with the dispersion method values, but had more scatter about the median values. The increased scatter is probably due to small biases introduced by the various methods of interpolating the input light curves. The final check was to combine the input light curves by shifting the A, C, and D curves by the appropriate time delays and magnifications and then combining them with the unshifted B light curve. The resulting composite curves are shown in Figures 4–6. The composite curves show that the major features, and many of the minor features, in each of the individual light curves are reproduced in the other light curves at the proper times, giving additional confidence that the measured delays are the correct ones.

5. Uncertainties on Measured Delays

We have estimated the uncertainties on the time delays and relative magnifications through Monte Carlo simulations. This is the same method that was used in Paper I. To summarize, we smoothed each of the composite curves (Figures 4–6) to create the input “true” light curves for the simulations. One “true” light curve was generated for each season, using the best-fit relative magnifications appropriate for that season. The delays used for each season were the global time delays derived from the combined analysis (see Table 4 for the input delays and relative magnifications). The smoothing method used to generate the “true” curves from the composites was the variable-width boxcar technique described in Paper I, with five points in the smoothing window.

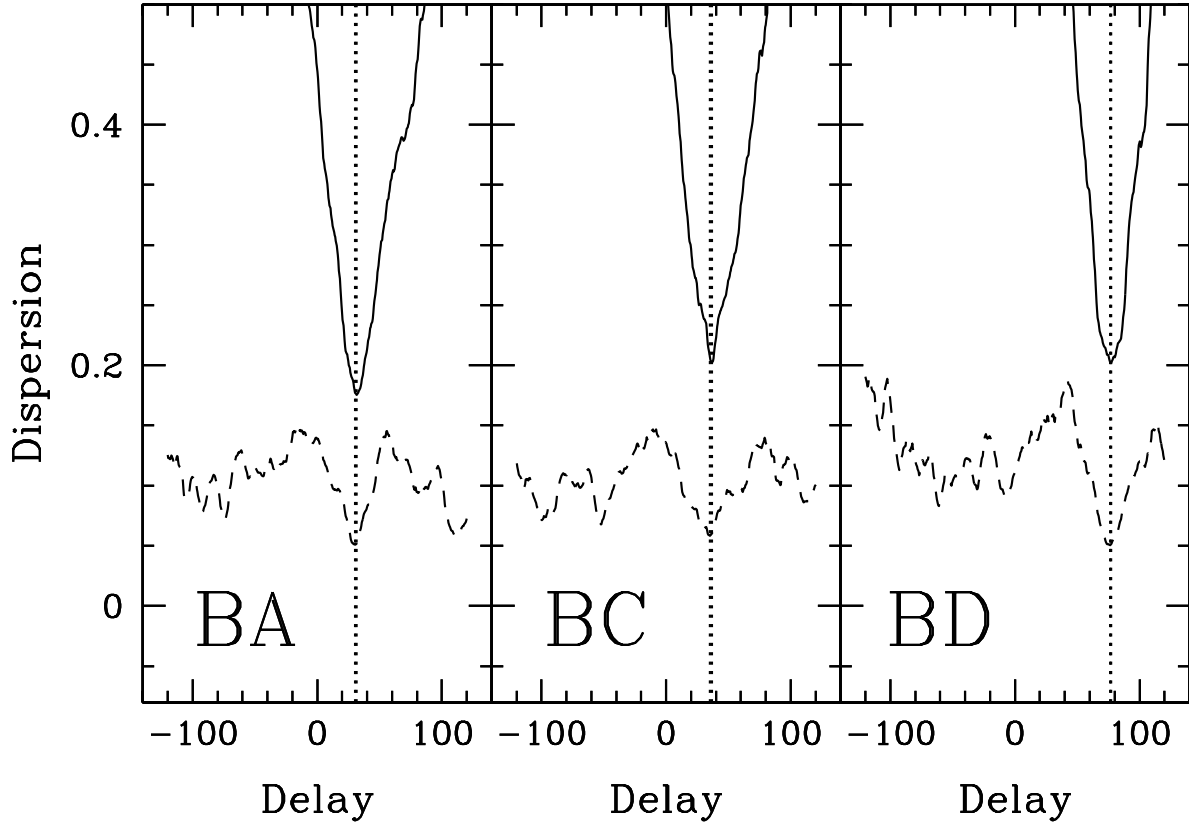


Fig. 3.— Dispersion spectra from comparison of the light curves of components B and A (left panel), B and C (middle panel), and B and D (right panel). The spectra were calculated with the D_4^2 method with $\delta = 5.5$ days (see §4.2). The curve minima, marked with vertical dotted lines, indicate the time delays. The solid curves represent the results from analysis of the combined data sets from all three seasons, while the dashed curves represent the results from season 1 alone.

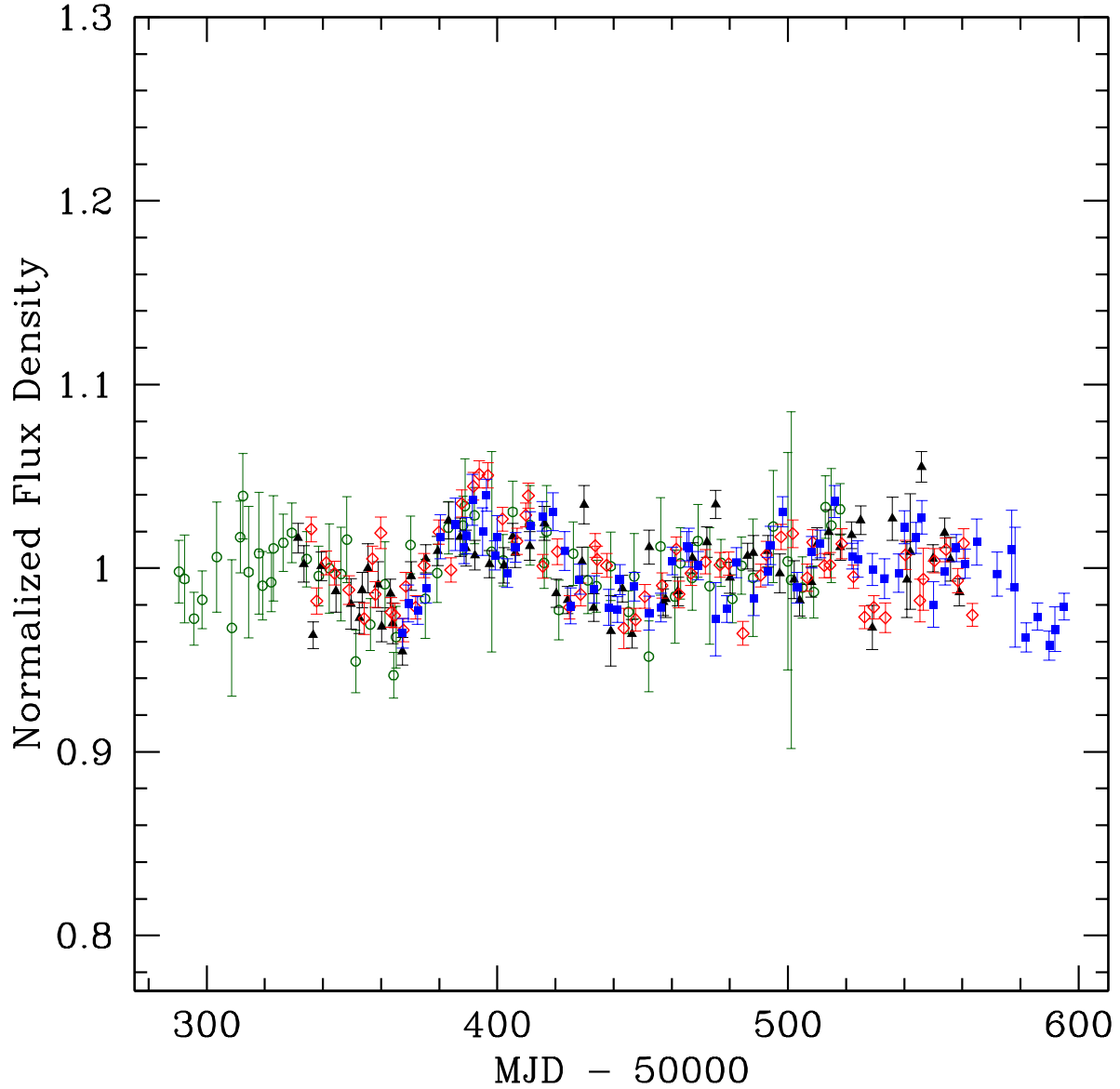


Fig. 4.— Composite light curve constructed from the recalibrated data from season 1. The light curves for components A, C, and D have been shifted by the time delays and relative magnifications given in Table 4 and overlaid on the component B light curve. The resulting curve was then normalized by its mean value. Component D is the faintest image and thus the fractional measurement errors in its flux density are larger than those of the other components. The data points associated with the four components are denoted by open diamonds (red) for A, filled squares (blue) for B, filled triangles (black) for C, and open circles (green) for D. The vertical scale is chosen to match those used in Figures 5 and 6.

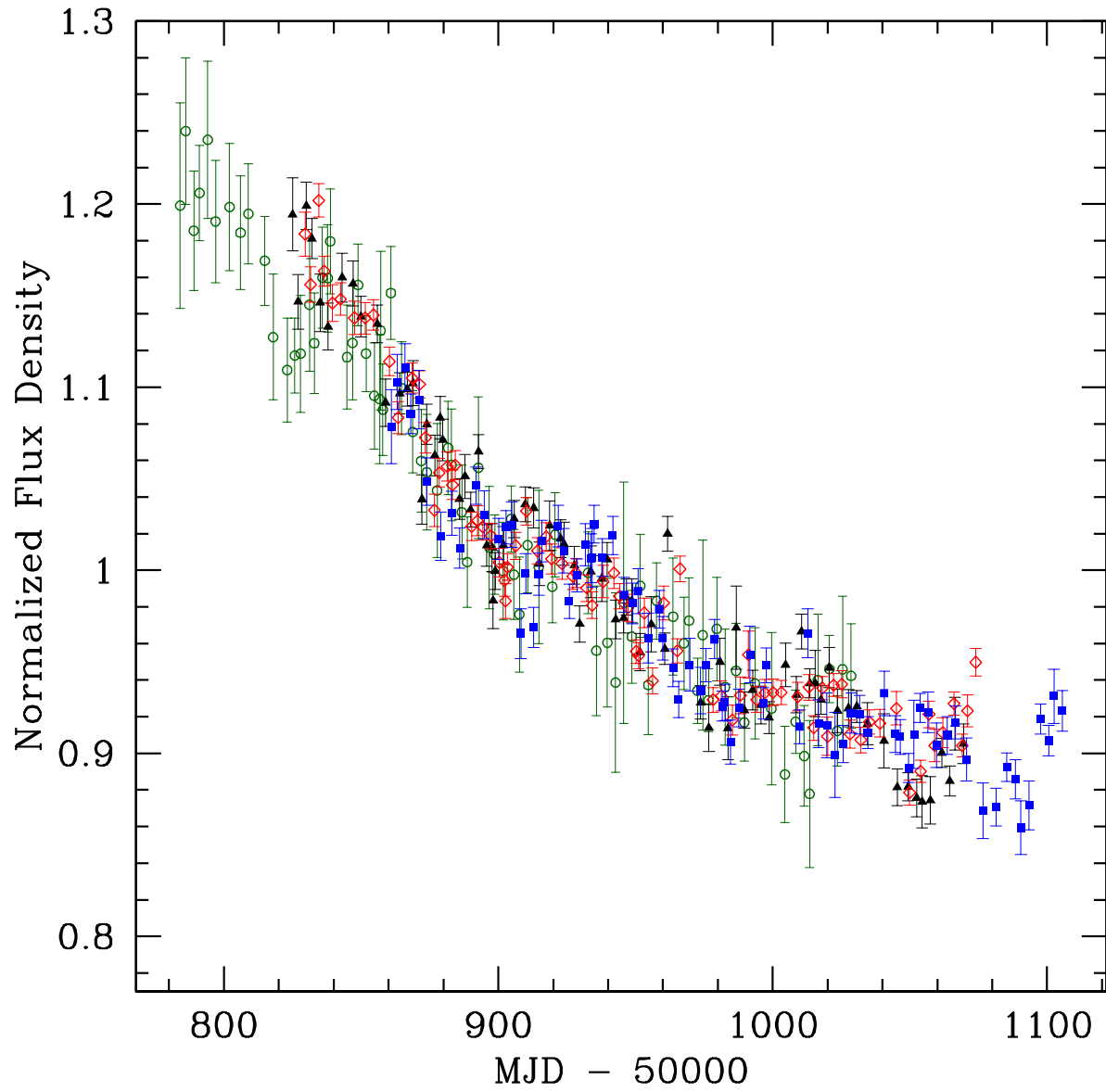


Fig. 5.— Same as Figure 4, but for the data from season 2.

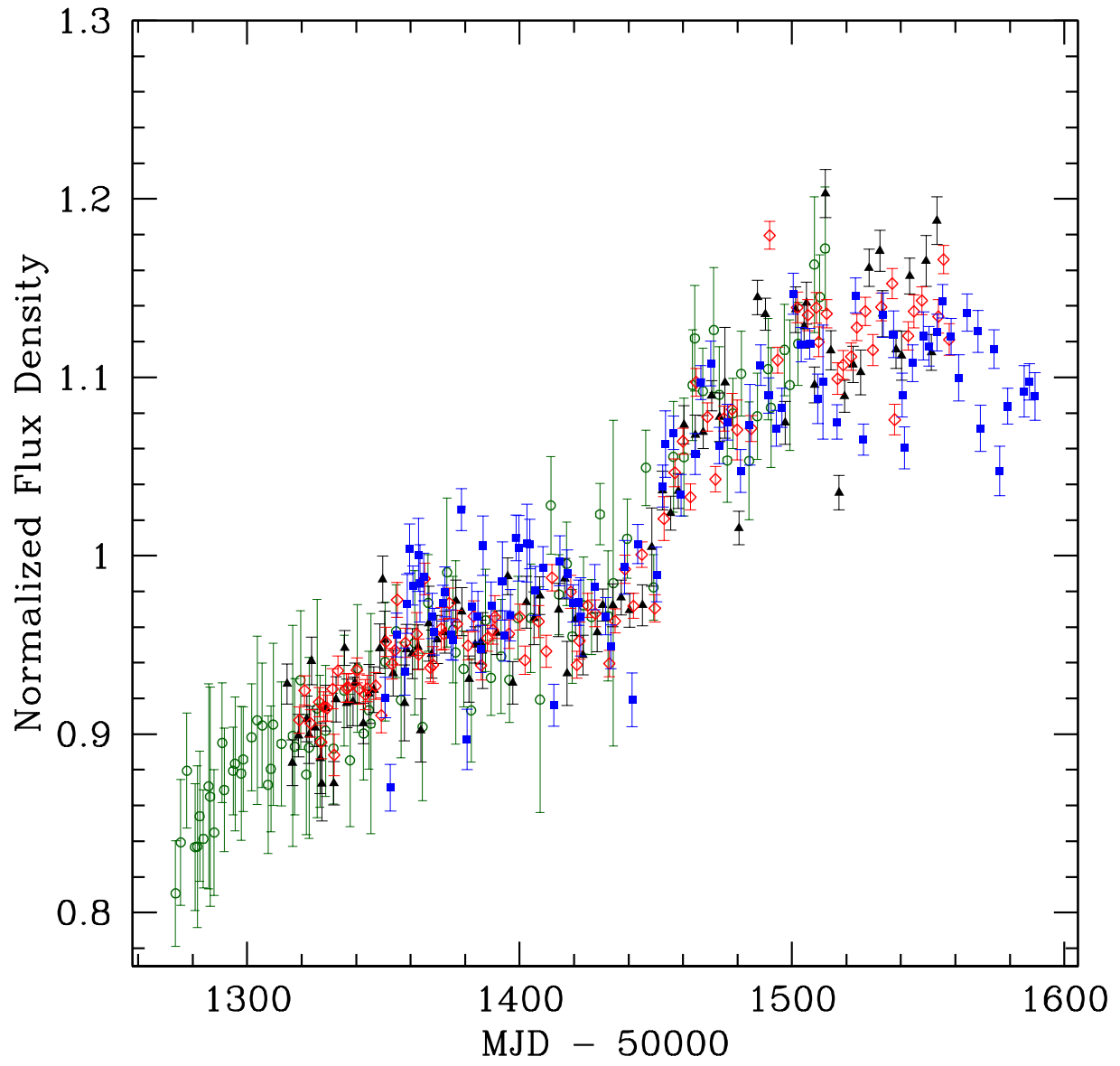


Fig. 6.— Same as Figure 4, but for the data from season 3.

The simulated light curves were created by adding a Gaussian-distributed random noise term to the points on the “true” curves. The widths of the Gaussian distributions, σ , were determined from the offsets between the measured composite curves and their smoothed counterparts. The values of σ used ranged from 1.4% to 1.9% of the mean flux densities of the lensed images. We generated 1000 Monte Carlo realizations of the data associated with each season.

The simulated light curves were analyzed with the same code used for the real light curves, using the $D_{4,2}^2$ method. The analysis was repeated using several different values of δ , with no significant difference in the results. The results in Table 5 were obtained for $\delta = 4.5\text{d}$. One advantage of the method used to analyze the monitoring data is that it yielded not only the time delays derived from the entire combined data set, but also the delays derived from each season individually. Thus, the effectiveness of the combined analysis can be evaluated. The distributions of time delays recovered from the simulations is shown in Figure 7, where the first three figures show the analyses of the individual seasons and the fourth shows the results from the combined data sets. The figures show that the distributions are non-Gaussian and that the season 2 data set does not constrain the time delays well. The latter result was expected given the nature of the light curves from that season. However, the analysis of the combined data set yields tight limits on the time delays, which are approximately a factor of two improvement on the limits derived from the season 1 data alone. All of the delays are now determined to $\pm 3\text{ d}$ or better (95% CL). The uncertainties on the delays and magnifications, as well as those on derived quantities, are given in Table 5.

6. Discussion

6.1. Evidence for Microlensing and Lens Substructure

As discussed in §4.2, the component relative magnifications were not constant from seasons 1 to 3. In particular, μ_{AB} and μ_{DB} decreased by 2% or more during the course of the observations (Figure 8). Although not large, these changes exceed the 95% confidence limits on the relative magnifications derived from the Monte Carlo simulations (Table 5), and thus appear to be real. Similar or more extreme changes in flux ratios are seen in optical monitoring of lens systems (e.g., Woźniak et al. 2000; Burud et al. 2000). These changes are attributed to microlensing events, where stars or other massive compact objects in the lensing galaxy change the magnifications of the lensed images as they move through the galaxy. For many years, it was thought that radio observations of gravitational lens systems should be unaffected by microlensing because the angular sizes of compact radio cores, typically on the order of a milliarcsecond, are much larger than the microarcsecond lensing cross sections of stars. However, radio monitoring of the lens CLASS B1600+434 has revealed changes in the component flux ratio that has been attributed to microlensing (Koopmans & de Bruyn 2000). In the case of B1600+434 the unexpected microlensing was interpreted as being due to the superluminal motion of a microarcsecond-sized component in the jet of the background

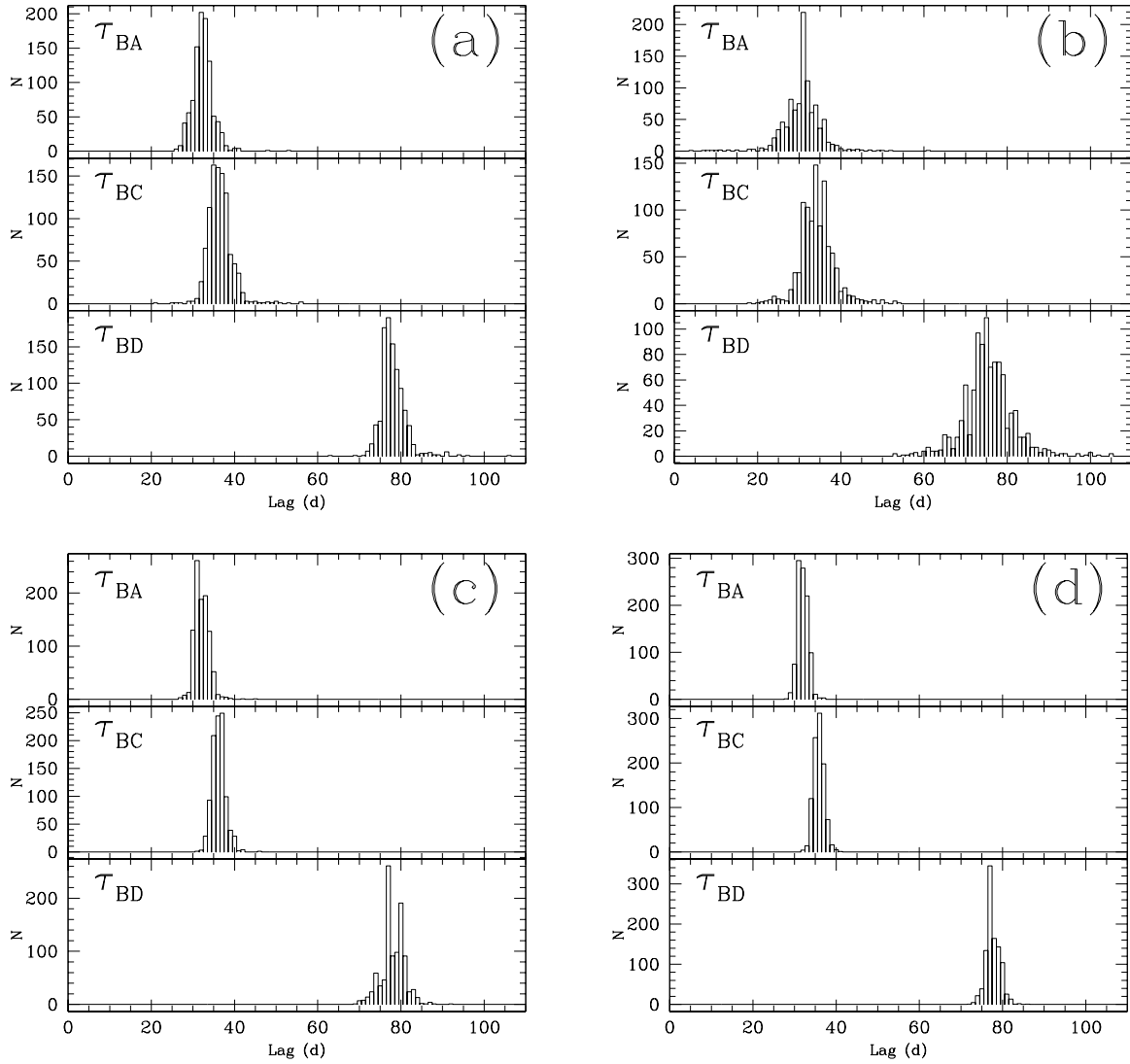


Fig. 7.— Distribution of time delays resulting from dispersion-method analysis of 1000 Monte Carlo realizations of the component light curves. (a) Season 1 results. (b) Season 2 results. (c) Season 3 results. (d) Results from the analysis of the combined data from all three seasons.

quasar across the complex caustic structure produced by compact objects in the lens galaxy halo (Koopmans & de Bruyn 2000). The lensed source in the B1608+656 system is the core of a classical radio double source (Snellen et al. 1995). Thus, it is certainly possible that there are extremely compact jet components associated with B1608+656 as well. On the other hand, the changes in the flux density ratios may have other explanations, such as scintillation. However, because we have monitored the system at only one frequency, we do not have the clear discriminant between microlensing and scintillation that multifrequency monitoring provides (Koopmans & de Bruyn 2000). With properly designed future observations, it may be possible to determine the cause of the changing flux density ratios in this system.

We note that, whatever the cause of the variability in the relative magnifications, it may also be necessary to invoke the presence of substructure in the B1608+656 lensing galaxies to explain the observed flux densities of the images. Simple, or even fairly complex, lens models of the B1608+656 system have not been able to properly reproduce all of the observed flux density ratios (Paper II; Myers et al. 1995). As we noted in Paper II, this discrepant magnification could be produced by perturbations to the smooth mass distributions assumed for the lensing galaxies. The presence of such substructure has been invoked to explain similarly discrepant flux ratios in other four-image lenses, although in those cases the incongruous ratios were those between bright merging images. In some cases, the substructure has been interpreted as globular clusters or plane density waves (Mao & Schneider 1998). Recently, several papers have suggested that the substructure is due to the small dark matter satellite halos expected from CDM structure-formation models (e.g., Metcalf & Madau 2001; Chiba 2002; Dalal & Kochanek 2002).

6.2. Determination of H_0 with B1608+656

To determine H_0 from a lens system, the measured time delays are combined with those predicted by the model. The predicted delays depend on the values of the fundamental cosmological parameters, so one must assume a cosmological model. Specifically, the model delays are proportional to $(D_\ell D_s)/D_{\ell s}$ where D_ℓ , D_s , and $D_{\ell s}$ are the angular diameter distances from the observer to the lens, from the observer to the source, and from the lens to the source, respectively. The angular diameter distances are functions of H_0 , Ω_m , and Ω_Λ , as well as the redshifts of the lens and the background source. We assume $(\Omega_M, \Omega_\Lambda) = (0.3, 0.7)$ for the rest of this paper. In comparison to this assumed cosmology, the value of H_0 derived from this lens system will change by no more than $\sim 6\%$ in both flat and open cosmological models with $0.1 < \Omega_M < 1.0$. As specific examples, the values of H_0 discussed below should be scaled by a factor of 1.02 if $(\Omega_M, \Omega_\Lambda) = (0.3, 0.0)$ and a factor of 0.94 if $(\Omega_M, \Omega_\Lambda) = (1.0, 0.0)$.

The considerable improvement in the accuracy of the measured time delays between the three image pairs in B1608+656 warrants an update of the lens model of this system, first presented in Paper II. Multiple time delays in a single lens system add additional constraints on the lens model, and an improvement in their accuracy could therefore lead to a change of the lens model and a

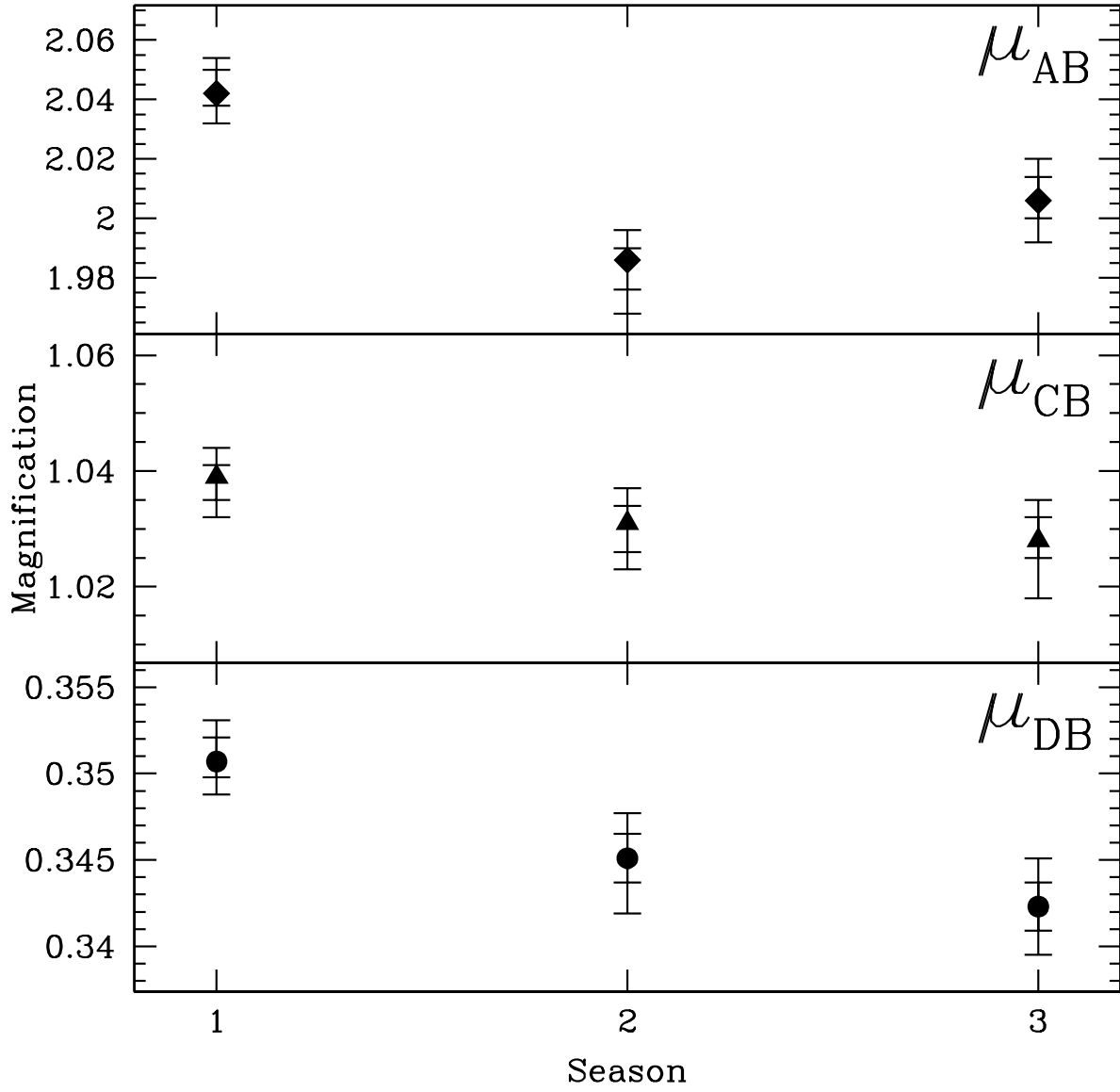


Fig. 8.— Relative magnifications with respect to component B as a function of the season of observations. For each point, the inner error bars are the 68% confidence regions from the Monte Carlo simulations, while the outer error bars are the 95% confidence regions.

change of the inferred Hubble Constant. Our models are based on the *lensmodel* package developed by Keeton (2001), but the results are consistent with those based on the code used in Paper II. We emphasize that the models presented here are only an update of the isothermal lens mass models in Paper II and that a much more detailed mass model will be presented in a forthcoming publication, where we fully exploit additional data on the system (see §7).

For the lens modeling in this paper, we use the same constraints as in Paper II. We use the VLBI image positions with formal 1σ errors listed in Paper II. Because the flux density ratios appear to slowly change in time (§4.2), even after the time-delay correction of the light curves, we widen the error bars to 20% on the flux density ratios to err on the side of caution. We use the improved time delays presented in this paper with 1.5 d errors (68% CL). We use singular isothermal ellipsoid (SIE) mass models for both lens galaxies (G1 and G2; see Paper II for details) and center them on the galaxy centroids measured from *Hubble Space Telescope* (HST) images obtained with the F555W, F814W, and F160W filters. The three centroids differ by amounts that are significant, which could be due to the presence of dust extinction and/or PSF problems. In addition, it is possible that the two merging lens galaxies are contained within a common dark matter halo and, thus, that the luminous material may not provide an accurate representation of the shape and centroid(s) of the mass distribution. These issues will be examined in more detail in the forthcoming publication. Here, we present models for the centroids from the F814W and F160W images; we reject the model based on the F555W centroids because it produces an extra image of the background source that is not seen in the data. As already shown in Paper II, the differences in the centroids do not strongly affect the inferred value of H_0 , although the cause of the wavelength-dependent shifts in position is something that requires further study.

The mass distributions of G1 and G2 are allowed to have a free mass scale (i.e., velocity dispersion), position angle, and ellipticity. At this point no external shear is allowed. Both lens galaxies are assumed to be at the same redshift. The results of the updated lens models and inferred values of H_0 are listed in Table 6. We note that these models are equivalent to models I and II in Table 3 of Paper II, in spite of using completely independent modeling codes in the two papers. We also note that, in order to compare the models produced by the two codes, it is important to understand how the mass scales in the models depend on the projected axial ratio of the lensing galaxies, q . We find that the relation between the quantities representing the lens strengths, σ in Paper II and b' in Table 6, is given by $b'\sqrt{1+q^2} \propto \sqrt{q}\sigma^2$. Using this relation, we find that the mass scales presented in Paper II and in Table 6 are also equivalent and that the mass ratio between galaxies G1 and G2 is $(M_1/M_2) \sim (b'_1/b'_2)^2 \sim 3$. This large mass ratio avoids the creation of additional images between galaxies G1 and G2.

We have also modeled the system with an allowance for an external shear (γ_{ext}). The addition of shear to the models in Table 6 leads to a considerable decrease in the value of χ^2 , for $\gamma_{\text{ext}} \sim 0.1$. However, the number of free parameters in the models increases to 11 (including H_0), and the models are less well constrained than the models with no shear. Additionally, although there are several small galaxies in the field around B1608+656, there is no evidence for a more massive group

or cluster that could yield a 10% external shear, as for example in the case of PG1115+080 (Kundić et al. 1997a; Tonry 1998). Thus, we think that the true external shear (i.e., a constant shear not due to the lens galaxies themselves) is unlikely to be as high as 10% and that a revision of the galaxy mass models is more likely required.

The formal statistical errors on H_0 in the models are $\pm 1 \text{ km s}^{-1} \text{ Mpc}^{-1}$ and $\pm 2 \text{ km s}^{-1} \text{ Mpc}^{-1}$ for the 1σ and 2σ confidence limits, respectively. In Paper II we estimated that the range of reasonable variations in the shapes of the mass profiles of the lens galaxies contributed an additional uncertainty of 30% to the determination of H_0 from this system. This estimate may be overly conservative, given the small scatter in mass profile slopes seen in other lens galaxies (§6.3). However, given the complex nature of the lens system and the uncertain positions of the lensing galaxies, we will use this estimate of the systematic modeling uncertainties in this paper. In §7, we discuss methods by which the modeling uncertainties for this system may be reduced.

We note that an alternative and independent approach to lens modeling, namely the non-parametric method developed by Williams & Saha (2000), produces estimates of H_0 and its systematic uncertainties that are similar to those determined in this paper. In comparison to the more frequently used analytic modeling approaches, the non-parametric method has the advantage of making fewer assumptions about the form of the mass distribution in the lensing galaxy or galaxies. Thus, it is possible to explore a larger region of the model space than is usually done with single analytic models and, as a consequence, to obtain a perhaps more realistic estimate of the uncertainties due to modeling. On the other hand, given the additional freedom in model parameters, the non-parametric approach may produce some descriptions of the lensing galaxy that do not have a physical meaning, in spite of the constraints introduced to produce realistic galaxy models. Therefore, a straightforward interpretation of the results may be difficult. Williams & Saha (2000) applied their approach to the B1608+656 system, using the image positions and time delays as constraints. The time delays used by Williams & Saha (2000) were from an early analysis of the Season 1 data and differ slightly from those found in this paper. However, these small differences should not significantly affect the resulting values of H_0 . Williams & Saha (2000) found that $\sim 90\%$ of their model reconstructions produced values of H_0 between 50 and 100 $\text{km s}^{-1} \text{ Mpc}^{-1}$. They also applied their non-parametric method to PG1115+080 and the results were combined with the B1608+656 results to produce $H_0 = 61 \pm 11 (\pm 18) \text{ km s}^{-1} \text{ Mpc}^{-1}$ at 68% (90%) confidence, for $(\Omega_M, \Omega_\Lambda) = (1.0, 0.0)$. For the cosmological model adopted in this paper, their value of H_0 would change to $65 \text{ km s}^{-1} \text{ Mpc}^{-1}$, consistent with our results.

6.3. Comparison to Determinations of H_0 with Other Lens Systems

Time delays have been measured in 11 lens systems, with the B1608+656 delays being among those with the smallest uncertainties. Unfortunately, the determination of H_0 from lenses is not as clean as one might have hoped. For nearly every lens with a measured time delay, more than

one model has been used to fit the data. Often the resulting values of H_0 are quoted with small formal errors that, when taken at face value, make different determinations of H_0 with the same lens system mutually exclusive at high levels of significance. These discrepant values of H_0 arise because observations of most lens systems do not tightly constrain the mass distribution of the lens, and there is a degeneracy between the steepness of the lens mass profile and the derived value of H_0 (e.g., Paper II; Williams & Saha 2000; Witt, Mao, & Keeton 2000).

Although it may not be possible to determine the radial mass profile in many individual lens systems, there are indications that lensing galaxies may follow a nearly universal mass profile. It is, for example, possible to assume that all lenses must give consistent determinations of H_0 and then use the time-delay measurements to obtain information about the mass distribution in the lenses. Kochanek (2002b) has performed this experiment on a sample of five lens systems with measured delays. He finds that, in order to produce the same value of H_0 , the mass surface density properties of the lensing galaxies must differ by only very small amounts. Furthermore, several independent lines of investigation indicate that not only are the mass distributions in many lenses similar, but that the mass profiles are close to isothermal. These approaches have used models that incorporate more data than the standard two or four image positions and fluxes. The additional inputs make it possible to place tight limits on the slope of the mass distribution. The additional constraints may come from full or partial Einstein rings (e.g., Kochanek 1995; Keeton et al. 2000; Kochanek et al. 2001), complex structure in the background source that is lensed into a ring-like configuration (Cohn et al. 2001), stellar dynamics (Treu & Koopmans 2002; Koopmans & Treu 2002), or the orientations of mas-scale jets seen in very high angular resolution radio maps (Rusin et al. 2002). Although it should not be concluded that all lens galaxies have nearly isothermal mass distributions, it may be that the range of mass profile slopes present in lensing galaxies is significantly smaller than what is allowed by the constraints in most individual lens systems with time delay measurements. If further observations strengthen these conclusions, then the contribution of a major source of systematic error in lens-derived measurements of H_0 may be significantly decreased.

The mass profile of the main lensing galaxy is not the only source of uncertainty in the determination of H_0 from a lens system. Another factor enters if there is a cluster or massive group associated with the primary lensing galaxy. The inclusion of the effects of the cluster can vastly complicate the lens model. The case of the first lens to be discovered, Q0957+561, is instructive. Despite many years of intensive observational and modeling efforts, no definitive model has been developed. For an excellent discussion of the wealth of historical models of this system, see Keeton et al. (2000). Clusters have also been discovered in association with RX J0911.4+0551 (Kneib, Cohen, & Hjorth 2000; Morgan et al. 2001) and possibly SBS 1520+530 (Faure et al. 2002). In addition, compact groups of galaxies have been discovered in association with several lens systems (e.g., Kundić et al. 1997a,b; Tonry 1998; Tonry & Kochanek 1999, 2000; Fassnacht & Lubin 2002; Rusin et al. 2001), although their effects on the lensing properties of the systems are much smaller than those of clusters. Still another problem in the determination of H_0 from gravitational lens systems arises if the location of the lensing galaxy is not known, as is the case in B0218+357 (Lehár

et al. 2000).

In spite of the possible problems mentioned above, the gravitational lens method is attractive because many of the systematic errors affecting the determination of H_0 with one lens system are different from those affecting other systems. Thus, it should be possible to obtain a global measurement of H_0 with small uncertainties by averaging the measurements from many lens systems. This is in contrast to the distance-ladder techniques in which many of the systematic uncertainties affect all distance determinations in the same sense. The major problem with the gravitational-lens method is that the number of lens systems with measured time delays is still small. Even though the number of systems for which delays have been measured has increased substantially over the last few years, some of the delays are not measured to high precision. In addition, lens models for some systems are viewed with suspicion due to problems such as those mentioned in the previous paragraph. Thus, efforts to determine a global value of H_0 often exclude a significant fraction of systems with time-delay measurements. Recent attempts have been limited to samples consisting of five or fewer lenses, and have obtained global values of H_0 ranging from ~ 50 to ~ 75 km s⁻¹ Mpc⁻¹ (e.g., Paper II; Schechter 2000; Kochanek 2002a). With such small sample sizes, the mean H_0 obtained can easily be biased by unknown factors affecting one or two of the lens systems. It is thus crucial to measure time delays in more lens systems in order to obtain a robust global determination of H_0 from lenses.

6.4. Comparison to Determinations of H_0 with Other Methods

There are, of course, methods for measuring H_0 that are completely independent of the lens-derived values. These include the traditional distance-ladder methods in which Cepheid-based distances are used to calibrate secondary distance indicators. The HST Key Project combined several secondary distance measurement methods to obtain a final value of $H_0 = 72 \pm 3(1\sigma) \pm 7$ (sys) km s⁻¹ Mpc⁻¹ (Freedman et al. 2001). Using an analysis of Cepheid-calibrated distances to Type Ia supernovae, Parodi et al. (2000) derived $H_0 = 59 \pm 6$ km s⁻¹ Mpc⁻¹ (2σ random errors combined with estimated systematic effects). The use of the Sunyaev-Zeldovich (SZ) effect is another approach that, like the gravitational lens method, is independent of the distance-ladder approach. In recent work by Mason, Myers, & Readhead (2001), the average measurement obtained from a flux-limited sample of clusters was $H_0 = 66_{-11}^{+14}(1\sigma) \pm 14$ (sys) km s⁻¹ Mpc⁻¹. The global values of H_0 determined from lenses, the SZ effect, and traditional distance-ladder methods are broadly consistent with each other and with the H_0 determined from B1608+656. The sources of systematic error in each of these methods are different. Therefore, if the methods all produced values of H_0 that were in good, rather than broad, agreement, the confidence that the correct value had been measured would be increased. It is important that steps be taken to understand the systematic errors affecting each method and to attempt to reduce those errors. The systematic errors associated with the gravitational lens method may be reduced if time delays can be measured and mass profiles can be determined in significantly larger samples of lens systems.

7. Summary and Future Work

In this paper we have presented data obtained during three seasons of monitoring of the B1608+656 gravitational lens system. An analysis of the combined data sets from the three seasons has led to an improvement of factors of two to three in the precision of the three time delays measured. In addition, there is evidence that the relative magnifications of the lensed images are changing. Because these relative magnifications should be independent of the absolute flux density calibration, the observed changes may imply that at least one of the images is being affected by microlensing. If this is the case, B1608+656 would be only the second lens system in which radio microlensing has been detected. A combination of the time delays with revised lens models yields $H_0 = 61\text{--}65 \text{ km s}^{-1} \text{ Mpc}^{-1}$, depending on the positions used for the lensing galaxies, for $(\Omega_M, \Omega_\Lambda) = (0.3, 0.7)$. These values decrease by 6% for $(\Omega_M, \Omega_\Lambda) = (1.0, 0.0)$. The uncertainties on H_0 due to the time delay measurements are ± 1 (± 2) $\text{km s}^{-1} \text{ Mpc}^{-1}$ for the 1σ (2σ) confidence intervals. Now that the time delays have been determined to 4–10% (95% CL), the dominant source of error in the determination of H_0 with the B1608+656 system comes from the lens model. The model uncertainties are on the order of $\pm 15 \text{ km s}^{-1} \text{ Mpc}^{-1}$.

There are two lensing galaxies within the ring of images in the B1608+656 system, which presents a challenge to the modeling process. Because of the disturbed nature of the system, discussions of general time delay properties and the derivation of H_0 from lenses have tended to discard B1608+656 from the samples being considered (e.g., Witt, Mao, & Keeton 2000; Kochanek 2002a). However, the B1608+656 system does have the advantage of having a nearly complete Einstein ring that is seen in optical and infrared HST images (Jackson et al. 1997; Surpi & Blandford 2002). It thus may be possible to use the ring data to constrain the mass profile slopes of the lensing galaxies. Techniques to incorporate the Einstein ring data into the B1608+656 model have been described by Blandford, Surpi, & Kundić (2001) and Kochanek et al. (2001). The observed ring is faintest between components B and D, and is not detected at high significance in this region in the available HST images (Kochanek et al. 2001; Surpi & Blandford 2002). In order to fully exploit the ring modeling techniques, it is critical to obtain deeper HST images of the system so that the ring emission can be more clearly separated from the noise. The availability of the new Advanced Camera for Surveys, with improved sensitivity and a finer pixel scale compared to the Wide Field Planetary Camera 2, and the revived Near Infrared Camera and Multi-Object Spectrometer will greatly aid in the effort to get such images. In addition to the analysis of Einstein ring emission, information about the stellar dynamics of lensing galaxies can place strong constraints on the mass distribution of the lens (Treu & Koopmans 2002; Koopmans & Treu 2002). We have obtained high resolution spectra of the B1608+656 system with the Echelle Spectrograph and Imager on the Keck II telescope with which we will investigate the dynamics of the lensing galaxies. A full analysis of the Einstein ring structure, the environment surrounding the lens system, and the stellar kinematics should help to break the remaining degeneracies in the model (e.g., precise galaxy positions, external shear, radial mass profile, etc.) and, thus, significantly reduce the uncertainties on H_0 due to the lens model.

An observing program of this complexity could not have been completed without the assistance of the NRAO staff. Their efforts in keeping the VLA running smoothly and their advice on the structure of the observing program were invaluable. We especially thank Meri Stanley, Jason Wurnig, and Ken Hartley for making sure that all epochs had been properly scheduled. We are also grateful to the VLA operators for implementing the observing program. For useful discussions and comments on the paper, we thank Ingunn Burud, Stefano Casertano, Tim Pearson, Lori Lubin, Steve Myers, Frazer Owen, Rick Perley, Ken Sowinski, and Greg Taylor. We thank the anonymous referee for suggestions that improved the paper.

Table 2. Component Positions and Mean Flux Densities

Component	x^a (arcsec)	y^a (arcsec)	$\langle S_1 \rangle$ (mJy)	$\langle S_2 \rangle$ (mJy)	$\langle S_3 \rangle$ (mJy)
A	0.000	0.000	34.1	21.8	22.8
B	-0.738	-1.962	16.8	10.6	11.6
C	-0.745	-0.453	17.3	11.3	11.6
D	1.130	-1.257	5.9	4.0	3.7

^aComponent positions are given in Cartesian rather than astronomical coordinates.

Table 3. Results of Dispersion Analysis of Combined Data Set

Statistic	δ^a	τ_{BA}	$\mu_{AB,1}$	$\mu_{AB,2}$	$\mu_{AB,3}$	τ_{BC}	$\mu_{CB,1}$	$\mu_{CB,2}$	$\mu_{CB,3}$	τ_{BD}	$\mu_{DB,1}$	$\mu_{DB,2}$	$\mu_{DB,3}$
D_2^2	...	32.5	2.042	1.986	2.016	36.5	1.038	1.031	1.026	78.5	0.351	0.344	0.343
$D_{4,2}^2$	3.5	32.0	2.042	1.982	2.010	35.5	1.038	1.032	1.026	78.5	0.351	0.344	0.342
$D_{4,2}^2$	4.5	32.0	2.042	1.984	2.010	36.5	1.039	1.030	1.026	77.5	0.351	0.345	0.343
$D_{4,2}^2$	5.5	31.5	2.042	1.984	2.008	36.5	1.039	1.030	1.027	80.0	0.351	0.344	0.344
$D_{4,2}^2$	6.5	31.5	2.042	1.984	2.008	35.5	1.038	1.031	1.027	80.0	0.351	0.344	0.344
$D_{4,2}^2$	7.5	31.5	2.042	1.984	2.006	35.5	1.039	1.031	1.028	80.0	0.351	0.344	0.344
$D_{4,2}^2$	8.5	31.5	2.042	1.984	2.008	36.5	1.039	1.029	1.028	78.0	0.351	0.345	0.343
$D_{4,2}^2$	9.5	31.5	2.042	1.986	2.006	36.5	1.039	1.030	1.029	78.0	0.351	0.345	0.343
$D_{4,2}^2$	10.5	31.5	2.042	1.986	2.006	35.5	1.039	1.031	1.028	77.0	0.351	0.345	0.342
$D_{4,2}^2$	11.5	31.0	2.044	1.986	2.004	35.5	1.039	1.031	1.028	77.0	0.351	0.345	0.343
$D_{4,2}^2$	12.5	31.5	2.044	1.986	2.006	36.0	1.039	1.031	1.028	77.5	0.351	0.345	0.343
$D_{4,2}^2$	13.5	31.0	2.044	1.988	2.006	36.0	1.039	1.031	1.029	77.0	0.351	0.345	0.342
$D_{4,2}^2$	14.5	31.5	2.042	1.988	2.004	35.5	1.039	1.031	1.028	77.0	0.351	0.345	0.342
$D_{4,2}^2$	15.5	31.5	2.044	1.986	2.006	36.0	1.039	1.031	1.029	76.5	0.351	0.345	0.342
$D_{4,2}^2$	16.5	31.5	2.044	1.988	2.006	36.0	1.039	1.031	1.029	77.0	0.351	0.345	0.342
$D_{4,2}^2$	17.5	32.0	2.042	1.986	2.006	36.0	1.039	1.032	1.028	76.5	0.350	0.345	0.342
$D_{4,2}^2$	18.5	32.0	2.042	1.986	2.006	36.0	1.039	1.032	1.029	76.5	0.351	0.345	0.342
$D_{4,2}^2$	19.5	31.5	2.042	1.988	2.004	35.5	1.039	1.032	1.028	76.5	0.351	0.345	0.342
$D_{4,2}^2$	20.5	32.0	2.042	1.988	2.006	36.5	1.039	1.031	1.028	76.5	0.351	0.345	0.342

^aThe value of δ for the $D_{4,2}^2$ method (see §4.2).

Table 4. Measured Quantities

Component	τ^a	μ_1^b	μ_2^b	μ_3^b
A	31.5	2.042	1.986	2.006
C	36.0	1.039	1.031	1.028
D	77.0	0.351	0.345	0.342

^aTime delay between component in table and component B, in days.

^bRelative magnification of component in table with respect to component B, for season 1, 2, or 3.

Table 5. Parameter Confidence Intervals from Combined Analysis

Quantity	Input Value	68% Confidence Interval	95% Confidence Interval
τ_{BA}	31.5	30.5–33.5	29.0–34.5
τ_{BC}	36.0	34.5–37.5	33.5–38.5
τ_{BD}	77.0	76.0–79.0	74.0–81.0
$\mu_{AB,1}$	2.042	2.038–2.050	2.032–2.054
$\mu_{AB,2}$	1.986	1.976–1.990	1.968–1.996
$\mu_{AB,3}$	2.006	2.000–2.014	1.992–2.020
$\mu_{CB,1}$	1.039	1.035–1.041	1.032–1.044
$\mu_{CB,2}$	1.031	1.027–1.034	1.023–1.037
$\mu_{CB,3}$	1.028	1.025–1.032	1.021–1.035
$\mu_{DB,1}$	0.351	0.350–0.352	0.349–0.353
$\mu_{DB,2}$	0.345	0.344–0.347	0.342–0.348
$\mu_{DB,3}$	0.342	0.341–0.344	0.340–0.345
(τ_{BD}/τ_{BA})	2.44	2.37–2.47	2.34–2.51
(τ_{BD}/τ_{BC})	2.14	2.12–2.19	2.09–2.22

Table 6. Mass Model Parameters

Filter	x_c^a (arcsec)	y_c^a (arcsec)	b' (arcsec)	q	P.A. ^b (deg)	x_s^a (arcsec)	y_s^a (arcsec)	H_0 (km s ⁻¹ Mpc ⁻¹)	χ^2
F814W	+0.521	-1.062	0.68	0.88	+71.8	+0.060	-1.090	65	43
	-0.293	-0.965	0.39	0.39	+53.1				
F160W	+0.446	-1.063	0.69	0.91	-58.0	+0.058	-1.103	61	196
	-0.276	-0.937	0.36	0.31	+53.8				

^aPositions are given in Cartesian rather than astronomical coordinates.

^bPosition angles are defined in the astronomical convention, in degrees measured east of north.

Note. — Lens models for B1608+656 consisting of two SIE mass distributions with no external shear. Columns 2–3 indicate the galaxy centroids measured in the HST images obtained with the listed filter; columns 4–6 indicate the lens strength (see alpha models in Keeton 2001), axial ratio, and position angle of the SIE mass distribution; columns 7–8 indicate the source position; columns 9–10 indicate the inferred value of H_0 and the model χ^2 value. The values of H_0 are quoted for $(\Omega_M, \Omega_\Lambda) = (0.3, 0.7)$. Every first/second line indicates the parameters for galaxy G1/G1.

REFERENCES

- Barkana, R. 1997, *ApJ*, 489, 21
- Biggs, A. D., Browne, I. W. A., Helbig, P., Koopmans, L. V. E., Wilkinson, P. N., & Perley, R. A. 1999, *MNRAS*, 304, 349
- Blandford, R., Surpi, G., & Kundić, T. 2001, in *ASP Conf. Ser. 237, Gravitational Lensing: Recent Progress and Future Goals*, ed. T. G. Brainerd & C. S. Kochanek (San Francisco: ASP), 65
- Burud, I., et al. 2000, *ApJ*, 544, 177
- Burud, I., et al. 2002a, *A&A*, 383, 71
- Burud, I., et al. 2002b, *A&A*, in press (astro-ph/0206084)
- Chiba, M. 2002, *ApJ*, 565, 17
- Cohen, A. S., Hewitt, J. N., Moore, C. B., Haarsma, D. B. 2000, *ApJ*, 545, 578
- Cohn, J. D., Kochanek, C. S., McLeod, B. A., & Keeton, C. R. 2001, *ApJ*, 554, 1216
- Dalal, N. & Kochanek, C. S. 2002, *ApJ*, 572, 25
- Fassnacht, C. D., Womble D. S., Neugebauer, G., Browne, I. W. A., Readhead, A. C. S., Matthews, K., & Pearson, T. J. 1996, *ApJ*, 460, L103
- Fassnacht, C. D., Pearson, T. J., Readhead, A. C. S., Browne, I. W. A., Koopmans, L. V. E., Myers, S. T., & Wilkinson, P. N. 1999, *ApJ*, 527, 498 (Paper I)
- Fassnacht, C. D. & Taylor, G. B. 2001, *AJ*, 122, 1661 (FT01)
- Fassnacht, C. D. & Lubin, L. M. 2002, *AJ*, 123, 627
- Faure, C., Courbin, F., Kneib, J. P., Alloin, D., Bolzonella, M., & Burud, I. 2002, *A&A*, 386, 69.
- Freedman, W. L., et al. 2001, *ApJ*, 553, 47
- Gil-Merino, R., Wisotzki, L, & Wambsganss, J. 2002, *A&A*, 381, 428
- Hjorth, J., et al. 2002, *ApJ*, 572, L11
- Jackson, N. J., Nair, S., Browne, I. W. A. 1997, in *Observational Cosmology with the New Radio Surveys*, ed. M. Bremer, N. Jackson & I. Perez-Fournon, (Dordrecht: Kluwer) 315
- Keeton, C. R., et al. 2000, *ApJ*, 542, 74
- Keeton, C. R. 2001, *ApJ*, submitted (astro-ph/0102340)
- Kneib, J.-P., Cohen, J. G., & Hjorth, J. 2000, *ApJ*, 544, 35

- Kochanek, C. S. 1995, *ApJ*, 445, 559
- Kochanek, C. S., Keeton, C. R., & McLeod, B. M. 2001, *ApJ*, 547, 50
- Kochanek, C. S. 2002a, *ApJ*, submitted (astro-ph/0204043)
- Kochanek, C. S. 2002b, *ApJ*, submitted (astro-ph/0205319)
- Koopmans, L. V. E. & Fassnacht, C. D. 1999, *ApJ*, 527, 513 (Paper II)
- Koopmans, L. V. E. & de Bruyn, A. G. 2000, *A&A*, 358, 793
- Koopmans, L. V. E., de Bruyn, A. G., Xanthopoulos, E., & Fassnacht, C. D. 2000, *A&A*, 356, 391
- Koopmans, L. V. E. & Treu, T. 2002, *ApJ*, submitted (astro-ph/0205281)
- Kundić, T. et al. 1995, *ApJ*, 455, L5
- Kundić, T., Cohen, J. G., Blandford, R. D., & Lubin, L.M. 1997a, *AJ*, 114, 507
- Kundić, T., Hogg, D. W., Blandford, R. D., Cohen, J. G., Lubin, L. M., & Larkin, J. E. 1997b, *AJ*, 114, 2276
- Kundić, T. et al. 1997c, *ApJ*, 482, 75
- Lehár, J, Falco, E. E., Kochanek, C. S., McLeod, B. A., Muñoz, J. A., Impey, C. D., Rix, H.-W., Keeton, C. R., & Peng, C. Y. 2000, *ApJ*, 536, 584
- Lovell, J. E. J., Jauncey, D. L., Reynolds, J. E., Wieringa, M. H., King, E. A., Tzioumis, A. K., McCulloch, P. M., & Edwards, P. G. 1998, *ApJ*, 508, L51
- Mao, S. & Schneider, P. 1998, *MNRAS*, 295, 587
- Mason, B. S., Myers, S. T., & Readhead, A. C. S. 2001, *ApJ*, 555, 11
- Metcalf, R. B. & Madau, P. 2001, *ApJ*, 563, 9
- Morgan, N. D., Chartas, G., Malm, M., Bautz, M. W., Burud, I., Hjorth, J., Jones, S. E., & Schechter, P. L. 2001, *ApJ*, 555, 1
- Myers, S. T., et al. 1995, *ApJ*, 447, L5
- Parodi, B. R., Saha, A., Sandage, A., & Tammann, G. A. 2001, *ApJ*, 551, 973
- Patnaik, A. R., & Narasimha, D., 2001, *MNRAS*, 326, 1403
- Pelt, J., Hoff, W., Kayser, R., Refsdal, S., & Schramm, T. 1994, *A&A*, 286, 775
- Pelt, J., Kayser, R., Refsdal, S., & Schramm, T. 1996, *A&A*, 305, 97

- Pelt, J., Refsdal, S., & Stabell, R. 2002, A&A, in press (astro-ph/0205424)
- Refsdal, S. 1964, MNRAS, 128, 307
- Rusin, D., et al. 2001, ApJ, 557, 594
- Rusin, D., Norbury, M., Biggs, A. D., Marlow, D. R., Jackson, N. J., Browne, I. W. A., Wilkinson, P. N., & Myers, S. T. 2002, MNRAS, 330, 205
- Schechter, P. L. 2000, to appear in ASP Conf. Ser., New Cosmological Data and the Values of the Fundamental Parameters, ed. A. Lasenby, A. Wilkinson, & A. W. Jones (San Francisco: ASP) (astro-ph/0009048)
- Schechter, P. L., et al. 1997, ApJ, 475, L85
- Shepherd, M. C. 1997, in ASP Conf. Ser. 125, Astronomical Data Analysis Software and Systems VI, ed. G. Hunt & H. E. Payne, (San Francisco: ASP), 77
- Snellen, I. A. G., de Bruyn, A. G., Schilizzi, R. T., Miley, G. K. & Myers, S. T. 1995, ApJ, 447, L9
- Surpi, G. & Blandford, R. D. 2002, ApJ, submitted (astro-ph/0111160)
- Tonry, J.L. 1998, AJ, 115, 1
- Tonry, J. L. & Kochanek, C. S. 1999, AJ, 117, 2034
- Tonry, J. L. & Kochanek, C. S. 2000, AJ, 119, 1078
- Treu, T. & Koopmans, L. V. E. 2002, ApJ, 575, 87
- Wiklind, T. & Combes, F. 2001, in ASP Conf. Ser. 237, Gravitational Lensing: Recent Progress and Future Goals, ed. T. G. Brainerd & C. S. Kochanek (San Francisco: ASP), 155 (astro-ph/9909314)
- Williams, L. L. R. & Saha, P. 2000, AJ, 119, 439
- Witt, H. J., Mao, S., & Keeton, C. R. 2000, ApJ, 544, 98
- Woźniak, P. R., Udalski, A., Szymański, M., Kubiak, M., Pietrzyński, G., Soszyński, I., & Żebruń, K. 2000, ApJ, 540, L65